HHS Public Access

Author manuscript

Cell Rep. Author manuscript; available in PMC 2020 August 10.

Published in final edited form as:

Cell Rep. 2020 June 30; 31(13): 107791. doi:10.1016/j.celrep.2020.107791.

MZT Proteins Form Multi-Faceted Structural Modules in the γ-Tubulin Ring Complex

Michal Wieczorek[1,6], **Tzu-Lun Huang**[3,4,6], **Linas Urnavicius**[1,2,6], **Kuo-Chiang Hsia**[3,4,5,*], **Tarun M. Kapoor**[1,7,*]

[1]Laboratory of Chemistry and Cell Biology, The Rockefeller University, 1230 York Avenue, New York, NY 10065, USA

[2]Laboratory of Cell Biology, The Rockefeller University, 1230 York Avenue, New York, NY 10065, USA

[3]Molecular and Cell Biology, Taiwan International Graduate Program, Academia Sinica, and National Defense Medical Center, Taipei, Taiwan

[4]Institute of Molecular Biology, Academia Sinica, Taipei 11529, Taiwan

[5]Institute of Biochemistry and Molecular Biology, College of Life Sciences, National Yang-Ming University, Taipei 11221, Taiwan

[6]These authors contributed equally

[7]Lead Contact

SUMMARY

Microtubule organization depends on the γ-Tubulin ring complex (γ-TuRC), a ~2.3-MDa nucleation factor comprising an asymmetric assembly of γ-Tubulin and GCP2-GCP6. However, it is currently unclear how the γ-TuRC-associated microproteins MZT1 and MZT2 contribute to the structure and regulation of the holocomplex. Here, we report cryo-EM structures of MZT1 and MZT2 in the context of the native human γ-TuRC. MZT1 forms two subcomplexes with the N-terminal α-helical domains of GCP3 or GCP6 (GCP-NHDs) within the γ-TuRC "lumenal bridge." We determine the X-ray structure of recombinant MZT1/GCP6-NHD and find it is similar to that within the native γ-TuRC. We identify two additional MZT/GCP-NHD-like subcomplexes, one of which is located on the outer face of the γ-TuRC and comprises MZT2 and GCP2-NHD in complex with a centrosomin motif 1 (CM1)-containing peptide. Our data reveal how MZT1 and

*Correspondence: khsia@gate.sinica.edu.tw (K.-C.H.), kapoor@rockefeller.edu (T.M.K.).

AUTHOR CONTRIBUTIONS

M.W., T.-L.H., L.U., K.-C.H., and T.M.K. conceived the experiments. M.W. and T.-L.H. designed constructs and purified proteins. M.W. and L.U. performed cryo-EM experiments, processed data, and built molecular models. T.-L.H. performed biochemical reconstitution of recMZT1/recGCP6-NHD. T.-L.H. and K.-C.H. determined the recMZT1/recGCP6-NHD crystal structure. M.W., T.-L.H., L.U., K.-C.H., and T.M.K. prepared the manuscript.

DECLARATION OF INTERESTS

The authors declare no competing interests.

SUPPLEMENTAL INFORMATION

Supplemental Information can be found online at https://doi.org/10.1016/j.celrep.2020.107791.

MZT2 establish multi-faceted, structurally mimetic “modules” that can expand structural and regulatory interfaces in the γ-TuRC.

Graphical Abstract

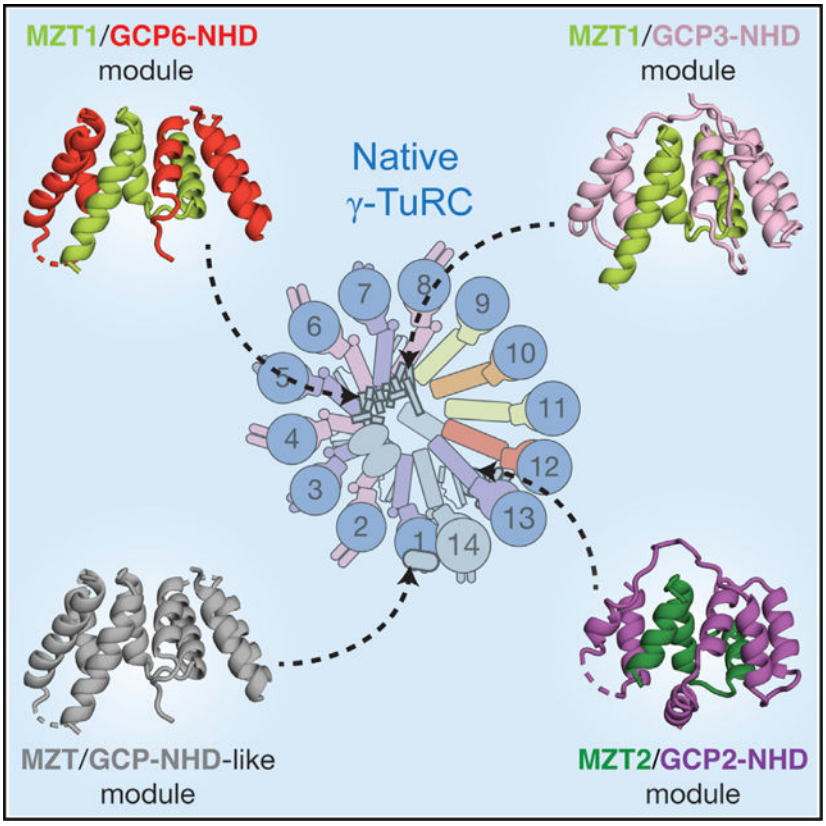

In Brief

Wieczorek et al. show how the microproteins MZT1 and MZT2 expand binding interfaces across the γ-TuRC—the cell’s microtubule nucleating machinery—by forming similarly shaped, “modular” subcomplexes with the α-helical N-terminal domains of different γ-Tubulin complex proteins (GCPs).

INTRODUCTION

Microtubules facilitate many fundamental cellular processes, including the trafficking of intracellular components and the faithful segregation of chromosomes (Forth and Kapoor, 2017; Vale, 2003). Microtubules are nucleated by the γ-Tubulin ring complex (γ-TuRC), a ~2.3-MDa assembly including the GTPase γ-Tubulin, the γ-Tubulin complex proteins 2–6 (GCP2–6) (Consolati et al., 2020; Liu et al., 2020; Moritz et al., 2000; Murphy et al., 2001; Stearns and Kirschner, 1994; Wieczorek et al., 2020; Zheng et al., 1995), and the mitotic-spindle organizing proteins associated with a ring of γ-Tubulin 1 and 2 (MZT1 and MZT2) (Hutchins et al., 2010).

MZT1 (initially called GIP-1) was discovered in *A. thaliana* as a GCP3-interacting protein (Janski et al., 2008). MZT1 and MZT2 were subsequently identified in human γ-TuRCs (Hutchins et al., 2010; Teixidó-Travesa et al., 2010), and both proteins have been consistently reported in biochemical analyses of vertebrate γ-TuRCs (Choi et al., 2010; Consolati et al., 2020; Liu et al., 2020; Thawani et al., 2018; Wieczorek et al., 2020). Although MZT1 depletion in cultured cells phenocopies the effects of γ-Tubulin RNAi (Hutchins et al., 2010), studies in fission yeast, *C. elegans*, *D. melanogaster*, *A. nidulans*, plant, and human cells have argued that MZTs are not required for γ-TuRC assembly; rather, they interact with GCPs to mediate γ-TuRC localization at specific microtubule organizing centers such as centrosomes (Sallee et al., 2018; Teixidó-Travesa et al., 2010), inner plaques of spindle pole bodies (Gao et al., 2019), basal bodies (Tovey et al., 2018), or pre-existing microtubules (Janski et al., 2012; Masuda et al., 2013; Nakamura et al., 2012). However, exactly how MZTs bind to γ-TuRCs is not clear.

One clue comes from studies of γ-TuRC "attachment factors," such as the pericentriolar protein CDK5Rap2 (Choi et al., 2010). CDK5Rap2 contains a conserved centrosomin motif 1 (CM1) found in several other γ-TuRC attachment factors, including *D. melanogaster* centrosomin, *S. cerevisiae* Spc72, and *S. pombe* Mto1 (Kollman et al., 2011; Tovey and Conduit, 2018). This motif has also been called the γ-TuRC nucleation activator (γ-TuNA), which in CDK5Rap2 is essential for maintaining the centrosomal localization of γ-TuRCs in cultured human cells (Choi et al., 2010). Importantly, previous microscale thermophoresis and immunoprecipitation studies have suggested a tripartite interaction among the γ-TuNA, MZT proteins, and GCPs (Lin et al., 2016), but the location of such a subcomplex in the γ-TuRC is not known.

Recent structures of native vertebrate γ-TuRCs demonstrated that the complex is built from two asymmetric halves: one containing multiple γ-Tubulin small complexes (γ-TuSCs) comprising γ-Tubulin, GCP2, and GCP3 located at positions 1–8 of the complex; and another containing an arrangement of GCP4, GCP5, GCP6, and a final γ-TuSC in an altered conformation (positions 9–14) (Consolati et al., 2020; Liu et al., 2020; Wieczorek et al., 2020) (Figure S1A). A substantial and unexpected density—the lumenal bridge—also spans across the inside of the γ-TuRC. The lumenal bridge contains an actin-like protein sandwiched between γ-Tubulins at γ-TuRC positions 2 and 3 on one side and a bundle of ~16 α helices on the other. While all three recent cryo-EM γ-TuRC structures report a lumenal bridge, the ~16 α-helical densities are unassigned (Consolati et al., 2020; Liu et al., 2020; Wieczorek et al., 2020) (Figure S1A). In addition, the MZTs have not been assigned to any portion of the γ-TuRC due to their small size (~8 kDa for MZT1 and ~16 kDa for MZT2), a lack of prior structural data, and ambiguities in connecting densities between secondary structure elements in unassigned regions of the complex.

Here, we acquire additional cryo-EM data for the human γ-TuRC, which allowed us to build *de novo* models of MZTs in the native complex. We identify two copies of MZT1 found in structurally mimetic subcomplexes: one copy associates with the N terminus of GCP3, and the other associates with GCP6. We reconstitute and solve the X-ray crystal structure for one of these subcomplexes, validating our cryo-EM findings. Our models lead to the identification of two additional MZT/GCP-like subcomplexes in the γ-TuRC distal to the

lumenal bridge, one of which comprises MZT2, GCP2, and the CM1 of a γ-TuRC attachment factor. Our results reveal that together with N-terminal portions of the GCPs, MZT1 and MZT2 form multi-faceted, structurally mimetic "modules" at diverse locations in the γ-TuRC.

RESULTS

MZT1 Forms a Small α-helical Bundle in the γ-TuRC Lumenal Bridge

MZT1 is an ~82-residue-long protein conserved across vertebrates (Hutchins et al., 2010; Janski et al., 2012; Nakamura et al., 2012). Secondary structure predictions suggest that MZT1 contains three short, contiguous α helices (Figures 1A and 1B). Helix H3 is also predicted to form a coiled-coil (Figure 1A), suggesting that MZT1 interacts with itself or other α-helical protein domains.

To locate MZT1 in the γ-TuRC, we examined the 16 unassigned α helices in our previous cryo-EM reconstruction of the γ-TuRC lumenal bridge (domain ii in Figure S1A; Wieczorek et al., 2020). Located adjacent to an actin-like protein (domain i in Figure S1A, domain ii lacks unambiguous connecting densities between the ~16 short α-helical elements (~10–20 residues each), which has precluded their assignment in published γ-TuRC reconstructions (Liu et al., 2020; Wieczorek et al., 2020; Consolati et al., 2020).

To overcome these challenges, we collected additional cryo-EM datasets for γ-TuRCs isolated from HeLa S3 cells and combined the resulting particles with those from our previous work (Wieczorek et al., 2020). We performed particle subtraction and focused 3D refinement to reconstruct the density surrounding the γ-TuRC lumenal bridge and position 13 (see below), as described previously (Figures S1B and S2A–S2C; Table S1; see Method Details) (Wieczorek et al., 2020). The resulting density maps have similar overall resolutions to those in our previous work (lumenal bridge $FSC_{0.143}$ = 3.6Å; position 13 $FSC_{0.143}$ = 4.5Å; Figure S2A), but, importantly, they exhibit improved local resolution (Figures S2B and S2C), particularly in the previously difficult-to-resolve connecting loops between α helices in lumenal bridge domain ii, which allowed part of this density to be segmented into contiguous polypeptide "submaps" (sub-maps A and B; Figures 1C and 1H).

Submap A revealed an arrangement of three short α helices (Figure 1C) consistent with secondary structure predictions for MZT1 (Figure 1A); gratifyingly, a *de novo* MZT1 model could be built and refined into this density (Figure 1D; Data S1; Table S2). The fit between model side chains and the corresponding density further validated MZT1's identity (Figure 1E; Data S1). The model accounts for ~95% of MZT1's primary sequence and reveals a three α-helix N-shaped fold (Figure 1D; Data S1). These results provide a model for human MZT1 and localize this small protein to the γ-TuRC lumenal bridge.

MZT1 Intercalates with a GCP3 N-Terminal Five-α-Helix Bundle

MZT1 is surrounded by multiple unassigned α-helical densities also found within domain ii (submap B; Figures 1H and S1A). A strong candidate protein for submap B is the N-terminal portion of one of GCP2, GCP3, GCP5, or GCP6, which were not accounted for in recent γ-TuRC reconstructions (Liu et al., 2020; Wieczorek et al., 2020; Consolati et al.,

2020). Secondary structure predictions suggest that these domains adopt a fold of typically five short (~10–15 residues) α helices in a motif we term the N-terminal α-helical domain (GCP-NHD; Figures 1F, 1G, and S3A). GCP3-NHD in particular has been shown to interact with MZT1 in cells and *in vitro* (Cota et al., 2017; Dhani et al., 2013; Janski et al., 2008, 2012; Leong et al., 2019; Lin et al., 2016; Nakamura et al., 2012; Tovey et al., 2018). Notably, submap B corresponds to a single polypeptide that contains five contiguous α helices and surrounds the MZT1 density (Figure 1H). Gratifyingly, a *de novo* model for GCP3-NHD could be built and refined into submap B (Figures 1I and 1J; Data S1; Table S2). Additionally, the C-terminal end of the GCP3-NHD model connects to a previously unassigned loop that snakes down the lower (N) domain of the GCP2 "stalk" at position 7 towards the bottom of GCP3 at position 6 (Figure S3F). This loop was therefore assigned to GCP3 residues ~113–129 (Figures S3G and S3H; Data S1; Table S2) and suggests that the GCP3-NHD in the lumenal bridge could stem from GCP3 at γ-TuRC position 6.

The GCP3-NHD model reveals a W-shaped fold that intercalates with MZT1 in an unusual α-helical dimerization motif (Figure 1K). The eight-α-helical subcomplex formed by MZT1 and GCP3-NHD (hereafter MZT1/GCP3-NHD) resembles a flattened pyramid and comprises 8 out of ~16 α helices inlumenal bridge domain ii (Figures 1K and 2A; hereafter domain ii-A), which are positioned adjacent to GCP3 (position 8), GCP4 (position 9), and GCP5 (position 10) (Figure S1A; Wieczorek et al., 2020). Part of the MZT1/GCP3-NHD interface comprises hydrophobic residues L28, I31, L44, and V48 from helices H1 and H2 of MZT1 and L81, I93, L94, and L97 from helices H4 and H5 of GCP3-NHD (Figure 1L). Together, our data show that MZT1 and GCP3-NHD form a compact, α-helical subcomplex in the γ-TuRC lumenal bridge.

A Second MZT1 and the N Terminus of GCP6 Occupy the Remainder of the Lumenal Bridge

We next examined the ~8 remaining unassigned α helices in lumenal bridge domain ii (hereafter, domain ii-B; Figure 2A), which contact MZT1/GCP3-NHD on one end and the actin-like protein on the other (Figure S1A). Remarkably, our model for MZT1/GCP3-NHD could be rigid-body fitted into the domain ii-B density (Figure 2B), suggesting a second copy of MZT1/GCP3-NHD occupies the lumenal bridge. However, while the side chains of a second MZT1 model fit the domain ii-B density (Figure 2D; Data S1; Table S2), the GCP3-NHD model did not (data not shown).

Instead, we discovered that a *de novo* model for GCP6-NHD could be built and refined into domain ii-B of the γ-TuRC lumenal bridge (Figures 2C and 2E; Data S1; Table S2). GCP6-NHD also adopts a W-shaped fold that intercalates with the second N-shaped MZT1 to form a subcomplex similar in size, shape, and topology to MZT1/GCP3-NHD (hereafter, MZT1/GCP6-NHD; root-mean-square deviation [RMSD] = 0.7Å; Figures S3B–S3E). Further, the C-terminal portion of GCP6-NHD connects to the previously identified γ-TuSC-associated α-helix that contacts several γ-TuSCs from positions 3–6 of the γ-TuRC (Liu et al., 2020; Wieczorek et al., 2020; Consolati et al., 2020). Consistent with secondary structure predictions and our assignment of GCP6-NHD in domain ii-B of the lumenal bridge, a *de novo* molecular model for GCP6 residues 130–195 could be built and refined into the γ-

TuSC-associated α-helix (hereafter, the GCP6 belt; Figures 2C and S3A; Data S1; Table S2). The GCP6 belt interacts with the γ-TuSCs via electrostatic interactions between GCP6 residues E157, E168, and E183 and clusters of basic residues at the lumenal side of the GCP2-GCP3 interfaces (Figures S3I–S3K). Supported by the assignment of the GCP6 belt, our results indicate that a second copy of MZT1 forms a subcomplex with GCP6-NHD that is similar in fold to MZT1/GCP3-NHD.

MZT1/GCP6-NHD interacts with MZT1/GCP3-NHD via GCP3-NHD helices H1 and H2 and GCP6-NHD helices H3 and H4 in a pseudo-C2 symmetry (Figure 2G). This interface contains a mixture of polar (e.g., GCP3-NHD residues Q33 and R37 and GCP6-NHD residues R67, D87, E90, and E94; Figure 2H) and non-polar contacts (e.g., GCP3-NHD F32 and V36 and GCP6-NHD L71 and F75; Figure 2I). The other end of MZT1/GCP6-NHD interacts with the actin-like protein at the barbed-end groove—a common binding site for actin-binding proteins (Pollard, 2016)—via GCP6-NHD helix H2 (Figure 2J). Though the identity of the actin-like protein is not yet established, GCP6-NHD contains at least two bulky hydrophobic residues (F46 and F50) proximal to hydrophobic and aromatic residues found in the barbed-end groove of the docked b-actin crystallographic model (e.g., Y143, I345, and L349; Figure 2K; Rould et al., 2006). Together, our results show that MZT1/GCP6-NHD is sandwiched between an actin-like protein and MZT1/GCP3-NHD to complete the γ-TuRC lumenal bridge (Figure 2L), and that MZT1 forms structurally mimetic subcomplexes with either GCP3-NHD or GCP6-NHD.

A MZT1/GCP6-NHD Subcomplex with a Native Fold Can Be Reconstituted *In Vitro*

To understand how the MZT1/GCP-NHD subcomplexes behave biochemically, we asked if one of them could be reconstituted. We generated bacterial expression constructs for full-length human MZT1 (recMZT1) and residues 1–119 of human GCP6 (recGCP6-NHD; Figure 3A; see Method Details). Initial purification tests indicated that recMZT1 and recGCP6-NHD are not soluble when expressed individually (data not shown). We therefore tested whether the co-overexpression of these two proteins could facilitate the formation of a stable recMZT1/recGCP6-NHD subcomplex (Figure 3B). Gratifyingly, this co-overexpression strategy yielded soluble recMZT1 and recGCP6-NHD that co-eluted as a single peak over a gel filtration column (Figures 3C and 3D). These data show that recMZT1 and recGCP6-NHD form a biochemically stable complex.

To further characterize purified recMZT1/recGCP6-NHD, we obtained crystals of the complex, which were used to generate a model by X-ray crystallography (3.3Å; Figure 3E; Table S3; PDB: 6M33; see Method Details). Remarkably, the crystallographic model of recMZT1/recGCP6-NHD revealed a near-identical fold to MZT1/GCP6-NHD cryo-EM model (RMSD = 1.4Å; Figure 3F). Both models indicate that the interface formed between MZT1 and GCP6-NHD totals ~2,200Å^2 and comprises hydrophobic residues in the core of the subcomplex (e.g., V110, L111, and L114; Figures 2F, S3D, and S3E), which have been shown to be important for a GCP6-MZT1 interaction from a previous yeast-two-hybrid analysis (Cota et al., 2017). These results validate our assignment of MZT1/GCP6-NHD in the γ-TuRC lumenal bridge and show that MZT1 and GCP6-NHD can form a stable complex independent of the γ-TuRC.

A Third MZT/GCP-NHD-Like Subcomplex Is Found at the γ-TuRC "Overlap"

The modular nature of the MZT1/GCP-NHD subcomplexes suggested they could occupy other unassigned densities in the γ-TuRC. We focused on the small (~2 × 2 × 3 nm) unassigned density found at the γ-TuRC "overlap" (Figures 3G, 3H, and S1A; Wieczorek et al., 2020). This density is located above γ-Tubulin at position 1 and adjacent to GCP3 at position 14 (Figures 3G and 3H). Limited resolution precluded *de novo* model building and assignment of protein(s) to the overlap density; however, in a recent cryo-EM study of the *X. laevis* γ-TuRC, some secondary structure elements are resolved in this region (Figure 3I) (Liu et al., 2020). Remarkably, our model for MZT1/GCP3-NHD could be rigid-body fitted into the overlap density of the *X. laevis* γ-TuRC (Figure 3J; Liu et al., 2020). Helices H1 and H3 of the docked MZT1 model each appear to protrude ~10Å past the observable density, suggesting the presence of another MZT1-like protein (e.g., MZT2; see below) or that the MZT1 α helices are dynamic. Nonetheless, our docking result shows that the overlap density corresponds to a third MZT1/GCP-NHD-like subcomplex.

MZT2 Adopts a MZT1-Like Fold and Interacts with GCP2 and a Dimeric Fragment of CDK5Rap2 on the Outer Face of the γ-TuRC

Lastly, we turned to the α-helical densities found at the outer face of the γ-TuRC at position 13 (GCP2) and adjacent to position 12 (GCP6; Figures 4A and 4B), previously termed the CC (coiled-coil) and HB (α-helical bundle) (Wieczorek et al., 2020). Remarkably, MZT1/GCP3-NHD could be rigid-body fitted into the HB density (Figure 4C). However, as with the overlap region (Figures 3G–3J), helices H1 and H3 of the docked MZT1 model extend ~10Å past the experimental density (Figure 4C). Further, a ~15-Å-long α-helical density extends from the C-terminal region of the docked GCP3-NHD model perpendicular to the other HB α helices (Figure 4C). This indicated that although the overall fold of the HB resembles the MZT1/GCP3-NHD subcomplex, likely neither MZT1 nor GCP3-NHD occupies the HB.

Instead, we considered MZT2, a small (~16 kDa) γ-TuRC protein that exists as two paralogs in human cells (MZT2A and MZT2B; ~96% identity), for the following reasons: (1) secondary structure predictions indicate that MZT2 likely adopts a contiguous 3–4-α-helical fold (Figures S4A and S4C; see Method Details); (2) after refinement into the HB density, a *de novo* C_β MZT2 model adopts a three-helix N-shaped fold (Figures 4D, 4F, and S4D; Table S4), suggesting that despite low (~20%) sequence identity between MZT1 and MZT2, there is structural conservation between these two proteins; and (3) MZT2 helices H1 and H3 are ~10Å shorter than those in MZT1 (Figure 4D), consistent with secondary structure predictions and the shorter length of the HB α-helical densities (Figures 4C, S4A, and S4C).These results collectively argue that MZT2 occupies the MZT1-like part of the HB.

To address the remaining ~6 α-helical HB densities, we examined secondary structure predictions of the GCP-NHDs. In contrast with GCP3-NHD (5 α helices), GCP2-NHD is predicted to contain six contiguous α helices (Figures S3A, S4B, and S4E), suggesting that GCP2-NHD occupies the remaining portion of the HB density. Several lines of evidence support this hypothesis: (1) the HB density directly contacts the GCP2 stalk at position 13 (Wieczorek et al., 2020); (2) an exclusive interaction between MZT2 and GCP2 has been

reported in a yeast-two-hybrid analysis (Lin et al., 2016); and (3) contacts between multiple residues in MZT2 helices H1 and H2 and in GCP2-NHD have recently been identified in a cross-linking mass spectrometry analysis of native human γ-TuRCs (Consolati et al., 2020). Motivated by this information, a C_β model for GCP2-NHD that is consistent with secondary structure predictions could be built and refined into the remaining portion of the HB density (Figures 4E and 4F; Table S4; see Method Details). Together, these observations are consistent with a model in which the HB region corresponds to a subcomplex of MZT2 and GCP2-NHD (MZT2/GCP2-NHD) that structurally mimics MZT1/GCP3-NHD.

MZT2/GCP2-NHD (the HB) also associates with an α-helical coiled-coil density (the CC; Figure 4B; Wieczorek et al., 2020). Notably, neither the HB nor CC densities at position 13 are observed in other reported γ-TuRC reconstructions (Consolati et al., 2020; Liu et al., 2020). This is likely due to our employment of the ~50-amino-acid fragment of CDK5Rap2 encompassing a conserved CM1 found in multiple γ-TuRC attachment factors—the so-called γ-TuNA (Choi et al., 2010)—to purify the γ-TuRC. Secondary structure predictions indicate that 60% of the γ-TuNA sequence forms an α-helical coiled-coil (Data S1). This suggested that a dimeric coiled-coil of γ-TuNA peptides occupies the CC density.

Taking advantage of the better-resolved side chain densities in the CC than the HB in our updated γ-TuRC density map (Figures S2A and S2C), a *de novo* atomic model for two copies of the γ-TuNA could be built into the CC (Figure 4G and 4H; Data S1; Table S4; see Method Details). We find that two γ-TuNA peptides form a ~30-residue-long dimeric, parallel, and left-handed coiled-coil (Figure 4G). As expected for an amphipathic coiled-coil, a string of hydrophobic residues line the γ-TuNA-γ-TuNA interface (Figure S4F). The coiled-coil is sandwiched between the MZT2/GCP2-NHD from the bottom and the GCP2 (position13) C-domain from the top (Figures 4G and 4J). Residues L79 and F75 from γ-TuNA helix A and GCP2 C-domain residues L614, V617, L618, M668, and L762 populate the CC/GCP2 C-domain interface (Figure 4I). In turn, γ-TuNA helix B contacts GCP2-NHD helices H1 and H2 (Figures 4G and S4H). Together, our data show that the γ-TuNA forms a dimeric coiled-coil that associates with MZT2/GCP2-NHD, and this tripartite subcomplex docks onto the outer face of the γ-TuRC.

DISCUSSION

In this study, we combine cryo-EM, biochemical reconstitutions, and X-ray crystallography to determine the structure of MZT proteins in the native human γ-TuRC. Our data show that γ-TuRCs contain at least four distinct, structurally mimetic subcomplexes, which we name MZT modules: (1) MZT1/GCP3-NHD and (2) MZT1/GCP6-NHD, both of which are found in the lumenal bridge; (3) a MZT/GCP-NHD-like module at the overlap density; and (4) MZT2/GCP2-NHD, which is found at position 13 in complex with two copies of the γ-TuNA (Figure 4K).

The MZT modules are built from 3 α helices contributed by a MZT (MZT1 or MZT2) intercalated with 5–6 α helices from a GCP-NHD (GCP2-NHD, GCP3-NHD, or GCP6-NHD; Figure 4K). The interface formed between MZT1 and GCP3/6-NHDs is surprisingly large for such small protein domains (~2,200$Å^2$ total; Figure S3C and S3E) and is mediated

by similar hydrophobic interactions between hydrophobic residues in MZT1 (e.g., L28 and I31 in helix H1) and relatively conserved residues in GCP-NHDs (e.g., I93, L94, and L97 in GCP3-NHD helix H5 and V110, L111, and L114 in GCP6-NHD helix H5; Figures 1L and 2F). This suggests that MZT1 can bind to different GCP-NHDs via similar hydrophobic interactions (Cota et al., 2017), explaining the reported lack of MZT1's specificity for different GCPs (Cota et al., 2017; Lin et al., 2016). Despite low (~20%) sequence similarity between MZT1 and MZT2, MZT2/GCP2-NHD forms a similar hydrophobic core in part between MZT2 and helix H5 of GCP2-NHD (Figure S4G). However, previous work suggested that MZT2 only interacts with GCP2 (Lin et al., 2016); this specificity may arise from contacts formed between MZT2 and GCP2-NHD helix H6, which is missing in the other GCP-NHDs (Figures 4E and 4F). It is also worth noting that our MZT2 model does not fit into the "staple" density on the outer face of each γ-TuSC (data not shown), which was recently assigned to MZT2 based on cross-linking mass spectrometry data (Consolati et al., 2020), suggesting the "staple" instead corresponds to an extension of the disordered GCP2 N terminus, as previously proposed (Wieczorek et al., 2020).

The MZT modules interact with the γ-TuRC not via the MZTs, but rather through the solvent-exposed surfaces of the GCP-NHD helices H1–H4 (Figures 2H–2K, 3J, and S4H). We note that compared with the GCP N- and C-domains (>30% identity; Murphy et al., 2001; Wieczorek et al., 2020), the GCP-NHDs are less conserved (<~10% identity), which may confer functional diversity to different MZT modules. As an example, the GCP6-NHD helix H2 is more structured than in GCP3-NHD, allowing it to point the bulky side chain of the GCP6-NHD-specific Phe50 toward the barbed-end groove of the actin-like protein (Figure 2K). Our results suggest that the solvent-exposed GCP-NHD residues will determine the specificity of a MZT module for its particular binding site within the γ-TuRC.

We also report that the CC density corresponds to the γ-TuNA, a fragment of CDK5RAP2, and one of several γ-TuRC attachment factors required for proper γ-TuRC localization in cells (Kollman et al., 2011). The γ-TuNA forms a dimeric coiled-coil that binds to MZT2/GCP2-NHD at the outer face of GCP2 on the asymmetric half of the γ-TuRC (position 13). Only one γ-TuNA dimer/MZT2/GCP2-NHD subcomplex is resolved at this position of the γ-TuRC, despite the presence of four more copies of GCP2 in the holocomplex (positions 1, 3, 5, and 7; Figures 4K and S1A), suggesting that MZT modules take advantage of the diverse interfaces provided by the asymmetric organization of γ-TuRC components (Wieczorek et al., 2020). The γ-TuNA contacts both the GCP2 C-domain (via γ-TuNA helix A; Figure 4I) and GCP2-NHD helices H1 and H2 in the MZT2/GCP2-NHD module (via γ-TuNA helix B; Figure S4H). γ-TuNA Phe75—a conserved hallmark of CM1 (Lin et al., 2014)—contributes to both of these interfaces (Figures 4I and S4H), potentially explaining why an F75A CDK5Rap2 mutant fails to rescue the loss of centrosomal γ-TuRC localization upon CDK5Rap2 depletion (Choi et al., 2010). Our models provide a template for studying how CM1-containing γ-TuRC attachment factors are recruited to the holocomplex at well-defined locations to establish diverse microtubule networks in cells.

Intriguingly, MZT1 is non-essential in *D. melanogaster* and is only expressed in testis (Tovey et al., 2018), and MZTs are absent in budding yeast (Kollman et al., 2011). Similarly, MZT2 is missing in plants, *D. melanogaster*, *C. elegans*, and fungi but is evolutionarily

conserved in the deuterostome lineage of animals (Kollman et al., 2011; Teixidó-Travesa et al., 2010). In an accompanying study, Huang et al. (2020 [this issue of Cell Reports]) also report crystal structures for MZT modules and demonstrate that the MZT1 homolog in *S. pombe* is dispensable for targeting γ-TuRCs to spindle poles during mitosis but is still essential for cell viability. These observations have led to a model in which γ-TuRCs exist in multiple compositional states, even within the same cell type, allowing cells to tune the γ-TuRC from a microtubule nucleator to a microtubule anchor (Gao et al., 2019; Muroyama et al., 2016; Sallee et al., 2018; Tovey et al., 2018). However, three recent, independent structures of vertebrate γ-TuRCs isolated using different affinity handles all display a well-defined lumenal bridge (Consolati et al., 2020; Liu et al., 2020; Wieczorek et al., 2020). Our findings demonstrate that in addition to their γ-TuRC-targeting roles in cells (Tovey and Conduit, 2018), MZT proteins constitute a significant portion of the γ-TuRC lumenal bridge, a prominent structural feature found in all native γ-TuRCs for which a near-atomic structure has been generated. In cells that lack the MZTs, similar modules may still form via evolutionary modifications of the GCP-NHDs or the presence of other, undiscovered MZT-like microproteins. Alternatively, the lumenal bridge—whose precise role in the γ-TuRC is not yet clear—may be dispensible for some γ-TuRC functions (e.g., microtubule nucleation) but essential for others (e.g., microtubule anchoring). Our study lays a structural foundation for studying how MZTs regulate the function of γ-TuRCs with mixed compositions.

STAR★METHODS

RESOURCE AVAILABILITY

Lead contact—Further information and requests for resources and reagents should be directed to and will be fulfilled by the Lead Contact, Tarun M. Kapoor.

Materials availability—All unique/stable reagents generated in this study are available from the Lead Contact without restriction.

Data and code availability—The accession numbers for the cryo-EM maps https://www.ebi.ac.uk/pdbe/emdb/ reported in this paper are: EMDB: EMD-21984 EMD-21985. The accession numbers for the structural models https://www.rcsb.org/ reported in this paper are: PDB: 6X0U, 6X0V, and 6M33.

EXPERIMENTAL MODEL AND SUBJECT DETAILS

HeLa S3 cell cytoplasmic extracts were prepared according to Abmayr and Carrozza (2001) and were a generous gift from Dr. Robert Roeder. Bacterial protein expression constructs were expressed in *Escherichia coli* BL21(DE3) pRIL or Rosetta cells cultured in LB medium supplemented with appropriate antibiotics at 37°C and at 230 rpm until induction, at which point the temperature was shifted to 16–18°C.

METHOD DETAILS

Purification of native human γ-TuRCs—GFP-γ-TuNA and GFP nanobody constructs were expressed and purified from *Escherichia coli* BL21(DE3) pRIL cells, as described previously (Wieczorek et al., 2020). Native γ-TuRCs were isolated from HeLa S3 cell

cytoplasmic extracts, a kind gift from Dr. Robert Roeder, based on the reported affinity of human γ-TuRCs for CDK5RAP2 (Choi et al., 2010), as described previously (Wieczorek et al., 2020).

Cryoelectron microscopy of native γ-TuRCs—2 μL of thawed γ-TuRCs was applied to plasma treated Quantifoil R2/2 300-square-mesh copper grids coated with a continuous carbon film. After 5–10 min the sample was blotted away and replaced with another 2 μL. This was repeated for a total of 5–8 applications. As γ-TuRC storage buffer contained ~30% (w/v) sucrose, 20 μL of washing buffer (40 mM HEPES-KOH pH 7.5, 150 mM KCl, 1 mM $MgCl_2$, 0.01% Tween-20 (v/v), 0.1 mM GTP, and 1 mM 2-mercaptoethanol) was used to rinse the grid twice with 1–2 min incubation in between. Finally, 3 μL of washing buffer was applied to the grid. The grid was transferred to a Vitroblot IV (FEI), blotted for 4–5 s at 100% humidity and 4°C, and then plunged into liquid ethane.

Micrographs were recorded on an FEI Titan Krios equipped with either a Gatan K2 Summit (Datasets 1 to 4) or Gatan K3 (Dataset 5; Table S1) detectors using Serial EM automated data collection (Mastronarde, 2005). Images were corrected for beam-induced drift using MotionCor2 (Zheng et al., 2017). CTF parameters for drift corrected micrographs were estimated using CTFFIND4 (Rohou and Grigorieff, 2015). Subsequent processing employed Relion v.3.0 (Zivanov et al., 2018), using a similar processing pipeline described previously in order to clean autopicked particles in Datasets 4 and 5 (Table S1; Wieczorek et al., 2020). The resulting “good” particles from Datasets 4 and 5 were combined with equivalent particles from Datasets 1 to 3 collected in our previous study (Wieczorek et al., 2020).

The combined particles were re-extracted using a pixel size of 1.036Å (instead of 1.335Å used in our previous study). Due to computational resource restraints, the box size was kept at 368 pixels, which resulted in some globular density at position 14 being close to the edge of both the box and circular masks. However, as this region could not be well-resolved due to high flexibility anyways (data not shown), this was not an issue for reconstructing the lumenal bridge or position 13 of the γ-TuRC in this study.

The combined, re-extracted particles were subjected to 3D refinement followed by 3D classification, resulting in 744,583 “final” particles selected for the final overall γ-TuRC refinement. Subsequently, particle subtraction followed by rounds of 3D focused classification and refinement were used to generate improved density maps for the lumenal bridge and the area surrounding position 13 (Figures S1B and S2), as described previously (Wieczorek et al., 2020).

Cryo-EM model building—The overall quality of side chain models generated in this study is summarized in Data S1. Jpred was used for secondary structure predictions (Drozdetskiy et al., 2015). LOMETS was used to generate *de novo* homology models of individual MZT1 and GCP-NHD α helices (Wu and Zhang, 2007). SWISS-MODEL was used to generate template-based homology models for GCP6-NHD (GCP3-NHD as template), MZT2 (MZT1 as template) and GCP2-NHD (GCP3-NHD as template) (Waterhouse et al., 2018). Because of limited side chain information, we could not distinguish between MZT2A and MZT2B paralogs and chose to use MZT2A for simplicity.

However, we note that within our modeled region of MZT2A, there is only one conservative amino acid change (G50A; found in the loop between helices H2 and H3) when the primary sequence is aligned to MZT2B (Teixidó-Travesa et al., 2010), suggesting that the core MZT-like fold adopted by both proteins is likely identical. An initial model for the γ-TuNA coiled-coil model was generated using CCBuilder 2.0 (Wood and Woolfson, 2018). All other *de novo*-built structural elements, as well as real-space refinements, were generated in Coot (Emsley et al., 2010) and refined using PHENIX (Adams et al., 2010; Williams et al., 2018).

Purification and X-ray crystallography of recMZT1/recGCP6-NHD—Codon optimized GCP6 residues 1–119 (NM_020461) were amplified and inserted into the pGEX-6p1 expression vector (GE Healthcare) that contains a PreScission cleavage site and a GST sequence to produce the N-terminal GST-fused proteins (recGCP6-NHD). recMZT1 was amplified by PCR and cloned into the pET-28a expression vector (GE Healthcare) to produce an N-terminal His-tagged protein. Both bacterial expression constructs were co-transformed into *Escherichia coli* Rosetta strain (Novagen). Protein production was induced by 0.5 mM IPTG at 18°C overnight. The cell pellet was resuspended in a buffer containing 20 mM HEPES (pH 7.4), 150 mM NaCl, and 3 mM DTT, disrupted by French press and clarified by centrifugation at 15,000 g at 4°C for 20 min. Clarified lysate was loaded onto a GST column (GE Healthcare), and GST bound proteins were digested by PreScission protease overnight at 4°C.

PreScission-digested samples were eluted and further purified by HiTrap Q (GE Healthcare). Protein was eluted by a NaCl gradient and then subjected to size exclusion chromatography (HiLoad 16/60 Superdex 75 prep gradeSuperdex 75 16/600 for crystal production, or Superdex 75 10/300 GL for analytical gel filtration as in Figure 3). The peak fractions were analyzed by SDS-PAGE. Purified protein fractions were collected and concentrated using Amicon Ultra 15 (Millipore) for crystallization. recMZT1/recGCP6-NHD crystals were grown in a 13 mg/ml protein concentration at 20°C in hanging drops containing 1 mL of the protein and 1 mL of a reservoir solution consisting of 6M ammonium nitrate and 0.1M Tris p.H 8.5. Proteins appeared as triclinic crystals (space group P 3221) that contain one molecule per asymmetric unit and diffract to ~3 Å. Data were collected at beamline 13B, 13C and 05A in the National Synchrotron Radiation Research Centre (Taiwan). X-ray intensities were processed using HKL2000 (Otwinowski and Minor, 1997). Phase determination was carried out using data collected from seleno-L-methionine-labeled crystals at selenium peak and inflection wavelengths using PHENIX (Adams et al., 2010). The initial model was built into the electron density map and refined using PHENIX and Coot (Adams et al., 2010; Emsley et al., 2010). The final structure was refined to a resolution of 3.3Å with an R-factor of 22.2% (Rfree 29.8%), and there were no outliers in the Ramachandran plot. Coordinates and structure factors have been deposited in the Protein Data Bank (Table S3).

Visualization and analysis—Figures were generated in PyMol (The PyMOL Molecular Graphics System, Version 2.0 Schrödinger, LLC.). Molecular graphics and analyses performed with UCSF Chimera, developed by the Resource for Biocomputing, Visualization, and Informatics at the University of California, San Francisco, with support

from NIH P41-GM103311 (Pettersen et al., 2004). Electrostatic potential coloring was performed in PyMol using the “vacuum electrostatics” function in PyMol. Hydrophobic coloring in Figure S4G was achieved using the “color_h.py” script in PyMol (https://www.expasy.org/tools/pscale/Hphob.Eisenberg.html) (Eisenberg et al., 1984). Structural alignments were performed using the “align” command in PyMol using the GCP-NHDs as the alignment reference. Protein-protein contact maps were generated using the COCOMAPS server (Vangone et al., 2011).

QUANTIFICATION AND STATISTICAL ANALYSIS

Resolution estimations of cryo-EM density maps are based on the 0.143 Fourier Shell Correlation (FSC) criterion (Rosenthal and Henderson, 2003). All statistical validation performed on the deposited models (PDB ID 6X0U, 6X0V, and 6M33) was done using the Phenix package (Tables S2–S4) (Williams et al., 2018).

Supplementary Material

Refer to Web version on PubMed Central for supplementary material.

ACKNOWLEDGMENTS

The authors thank Dr. R. Roeder for HeLa cell extracts and Dr. M. Rout for a GFP nanobody expression construct, as well as M. Ebrahim, J. Sotiris, and H. Ng for fantastic cryo-EM support. This work was funded by an NIH grant to T.M.K. (R35 GM130234). M.W. was supported by an HFSP fellowship (LT000025/18-L1). L.U. is supported by the Rockefeller University’s Pels Center for Biochemistry and Structural Biology. K.-C.H. acknowledges support from the Ministry of Science and Technology (MOST-106-2311-B-001-038-MY3) and Academia Sinica (AS-CDA-106-L02). Crystallographic technical services were provided by the Synchrotron Radiation Protein Crystallography Facility of the National Core Facility Program for Biotechnology, Ministry of Science and Technology and the National Synchrotron Radiation Research Center, a national user facility supported by the Ministry of Science and Technology of Taiwan, ROC.

REFERENCES

Abmayr SM, and Carrozza MJ (2001). Preparation of Nuclear and Cytoplasmic Extracts from Mammalian Cells In Current Protocols in Pharmacology, Enna SJ, Williams M, Ferkany JW, Kenakin T, Porsolt RD, and Sullivan JP, eds. (John Wiley & Sons, Inc.).

Adams PD, Afonine PV, Bunkóczi G, Chen VB, Davis IW, Echols N, Headd JJ, Hung L-W, Kapral GJ, Grosse-Kunstleve RW, et al. (2010). PHENIX: a comprehensive Python-based system for macromolecular structure solution. Acta Crystallogr. D Biol. Crystallogr 66, 213–221. [PubMed: 20124702]

Choi Y-K, Liu P, Sze SK, Dai C, and Qi RZ (2010). CDK5RAP2 stimulates microtubule nucleation by the gamma-tubulin ring complex. J. Cell Biol 191, 1089–1095. [PubMed: 21135143]

Consolati T, Locke J, Roostalu J, Chen ZA, Gannon J, Asthana J, Lim WM, Martino F, Cvetkovic MA, Rappsilber J, and Costa A (2020). Microtubule Nucleation Properties of Single Human γ-TuRCs Explained by Their Cryo-EM Structure. Developmental Cell. 53, 603–617. [PubMed: 32433913]

Cota RR, Teixidó-Travesa N, Ezquerra A, Eibes S, Lacasa C, Roig J, and Lüders J (2017). MZT1 regulates microtubule nucleation by linking γ-TuRC assembly to adapter-mediated targeting and activation. J. Cell Sci 130, 406–419. [PubMed: 27852835]

Dhani DK, Goult BT, George GM, Rogerson DT, Bitton DA, Miller CJ, Schwabe JWR, and Tanaka K (2013). Mzt1/Tam4, a fission yeast MOZART1 homologue, is an essential component of the γ-Tubulin complex and directly interacts with GCP3(Alp6). Mol. Biol. Cell 24, 3337–3349. [PubMed: 24006493]

Drozdetskiy A, Cole C, Procter J, and Barton GJ (2015). JPred4: a protein secondary structure prediction server. Nucleic Acids Res. 43, W389–94. [PubMed: 25883141]

Eisenberg D, Schwarz E, Komaromy M, and Wall R (1984). Analysis of membrane and surface protein sequences with the hydrophobic moment plot. J. Mol. Biol 179, 125–142. [PubMed: 6502707]

Emsley P, Lohkamp B, Scott WG, and Cowtan K (2010). Features and development of Coot. Acta Crystallogr. D Biol. Crystallogr 66, 486–501. [PubMed: 20383002]

Forth S, and Kapoor TM (2017). The mechanics of microtubule networks in cell division. J. Cell Biol 216, 1525–1531. [PubMed: 28490474]

Fridy PC, Li Y, Keegan S, Thompson MK, Nudelman I, Scheid JF, Oeffinger M, Nussenzweig MC, Fenyö D, Chait BT, and Rout MP (2014). A robust pipeline for rapid production of versatile nanobody repertoires. Nat. Methods 11, 1253–1260. [PubMed: 25362362]

Gao X, Schmid M, Zhang Y, Fukuda S, Takeshita N, and Fischer R (2019). The spindle pole body of *Aspergillus nidulans* is asymmetrical and contains changing numbers of γ-Tubulin complexes. J. Cell Sci 132, jcs234799. [PubMed: 31740532]

Huang T-L, Wang H-J, Chang Y-C, Wang S-W, and Hsia K-C (2020). Promiscuous binding of microprotein Mozart1 to γ-Tubulin complex mediates specific subcellular targeting to control microtubule array formation. Cell Rep. 31, Published online June 30, 2020. 10.1016/j.celrep.2020.107836.

Hutchins JRA, Toyoda Y, Hegemann B, Poser I, Hériché J-K, Sykora MM, Augsburg M, Hudecz O, Buschhorn BA, Bulkescher J, et al. (2010). Systematic Localization and Purification of Human Protein Complexes Identifies Chromosome Segregation Proteins. Science 328, 1181348.

Janski N, Herzog E, and Schmit A-C (2008). Identification of a novel small Arabidopsis protein interacting with gamma-tubulin complex protein 3. Cell Biol. Int 32, 546–548. [PubMed: 18178112]

Janski N, Masoud K, Batzenschlager M, Herzog E, Evrard J-L, Houlné G, Bourge M, Chabouté M-E, and Schmit A-C (2012). The GCP3-interacting proteins GIP1 and GIP2 are required for γ-Tubulin complex protein localization, spindle integrity, and chromosomal stability. Plant Cell 24, 1171–1187. [PubMed: 22427335]

Kollman JM, Merdes A, Mourey L, and Agard DA (2011). Microtubule nucleation by γ-Tubulin complexes. Nat. Rev. Mol. Cell Biol 12, 709–721. [PubMed: 21993292]

Leong SL, Lynch EM, Zou J, Tay YD, Borek WE, Tuijtel MW, Rappsilber J, and Sawin KE (2019). Reconstitution of Microtubule Nucleation In Vitro Reveals Novel Roles for Mzt1. Curr. Biol 29, 2199–2207.e10. [PubMed: 31287970]

Lin T-C, Neuner A, Schlosser YT, Scharf AND, Weber L, and Schiebel E (2014). Cell-cycle dependent phosphorylation of yeast pericentrin regulates γ-TuSC-mediated microtubule nucleation. eLife 3, e02208. [PubMed: 24842996]

Lin T-C, Neuner A, Flemming D, Liu P, Chinen T, Jäkle U, LArkowitziu R, and Schiebel E (2016). MOZART1 and γ-Tubulin complex receptors are both required to turn γ-TuSC into an active microtubule nucleation template. J. Cell Biol 215, 823–840. [PubMed: 27920216]

Liu P, Zupa E, Neuner A, Böhler A, Loerke J, Flemming D, Ruppert T, Rudack T, Peter C, Spahn C, et al. (2020). Insights into the assembly and activation of the microtubule nucleator γ-TuRC. Nature 578, 467–471. [PubMed: 31856152]

Mastronarde DN (2005). Automated electron microscope tomography using robust prediction of specimen movements. J. Struct. Biol 152, 36–51. [PubMed: 16182563]

Masuda H, Mori R, Yukawa M, and Toda T (2013). Fission yeast MOZART1/Mzt1 is an essential γ-Tubulin complex component required for complex recruitment to the microtubule organizing center, but not its assembly. Mol. Biol. Cell 24, 2894–2906. [PubMed: 23885124]

Moritz M, Braunfeld MB, Guénebaut V, Heuser J, and Agard DA (2000). Structure of the gamma-tubulin ring complex: a template for microtubule nucleation. Nat. Cell Biol 2, 365–370. [PubMed: 10854328]

Muroyama A, Seldin L, and Lechler T (2016). Divergent regulation of functionally distinct γ-Tubulin complexes during differentiation. J. Cell Biol 213, 679–692. [PubMed: 27298324]

Murphy SM, Preble AM, Patel UK, O'Connell KL, Dias DP, Moritz M, Agard D, Stults JT, and Stearns T (2001). GCP5 and GCP6: two new members of the human γ-Tubulin complex. Mol. Biol. Cell 12, 3340–3352. [PubMed: 11694571]

Nakamura M, Yagi N, Kato T, Fujita S, Kawashima N, Ehrhardt DW, and Hashimoto T (2012). Arabidopsis GCP3-interacting protein 1/MOZART 1 is an integral component of the γ-Tubulin-containing microtubule nucleating complex. Plant J 71, 216–225. [PubMed: 22404201]

Otwinowski Z, and Minor W (1997). Processing of X-ray diffraction data collected in oscillation mode. Methods Enzymol. 276, 307–326.

Pettersen EF, Goddard TD, Huang CC, Couch GS, Greenblatt DM, Meng EC, and Ferrin TE (2004). UCSF Chimera–a visualization system for exploratory research and analysis. J. Comput. Chem 25, 1605–1612. [PubMed: 15264254]

Pollard TD (2016). Actin and Actin-Binding Proteins. Cold Spring Harb. Perspect. Biol 8, a018226. [PubMed: 26988969]

Rohou A, and Grigorieff N (2015). CTFFIND4: Fast and accurate defocus estimation from electron micrographs. J. Struct. Biol 192, 216–221. [PubMed: 26278980]

Rosenthal PB, and Henderson R (2003). Optimal determination of particle orientation, absolute hand, and contrast loss in single-particle electron cryomicroscopy. J. Mol. Bio 333, 721–745. [PubMed: 14568533]

Rould MA, Wan Q, Joel PB, Lowey S, and Trybus KM (2006). Crystal structures of expressed non-polymerizable monomeric actin in the ADP and ATP states. J. Biol. Chem 281, 31909–31919. [PubMed: 16920713]

Sallee MD, Zonka JC, Skokan TD, Raftrey BC, and Feldman JL (2018). Tissue-specific degradation of essential centrosome components reveals distinct microtubule populations at microtubule organizing centers. PLoS Biol. 16, e2005189. [PubMed: 30080857]

Stearns T, and Kirschner M (1994). In vitro reconstitution of centrosome assembly and function: the central role of gamma-tubulin. Cell 76, 623–637. [PubMed: 8124706]

Tang G, Peng L, Baldwin PR, Mann DS, Jiang W, Rees I, and Ludtke SJ (2007). EMAN2: an extensible image processing suite for electron microscopy. J. Struct. Biol 157, 38–46. [PubMed: 16859925]

Teixidó-Travesa N, Villén J, Lacasa C, Bertran MT, Archinti M, Gygi SP, Caelles C, Roig J, and Lüders J (2010). The gammaTuRC revisited: a comparative analysis of interphase and mitotic human gammaTuRC redefines the set of core components and identifies the novel subunit GCP8. Mol. Biol. Cell 21, 3963–3972. [PubMed: 20861304]

Thawani A, Kadzik RS, and Petry S (2018). XMAP215 is a microtubule nucleation factor that functions synergistically with the γ-Tubulin ring complex. Nat. Cell Biol 20, 575–585. [PubMed: 29695792]

Tovey CA, and Conduit PT (2018). Microtubule nucleation by γ-Tubulin complexes and beyond. Essays Biochem. 62, 765–780. [PubMed: 30315097]

Tovey CA, Tubman CE, Hamrud E, Zhu Z, Dyas AE, Butterfield AN, Fyfe A, Johnson E, and Conduit PT (2018). γ-TuRC Heterogeneity Revealed by Analysis of Mozart1. Curr. Biol 28, 2314–2323.e6. [PubMed: 29983314]

Vale RD (2003). The molecular motor toolbox for intracellular transport. Cell 112, 467–480. [PubMed: 12600311]

Vangone A, Spinelli R, Scarano V, Cavallo L, and Oliva R (2011). COCO-MAPS: a web application to analyze and visualize contacts at the interface of biomolecular complexes. Bioinformatics 27, 2915–2916. [PubMed: 21873642]

Waterhouse A, Bertoni M, Bienert S, Studer G, Tauriello G, Gumienny R, Heer FT, de Beer TAP, Rempfer C, Bordoli L, et al. (2018). SWISS-MODEL: homology modelling of protein structures and complexes. Nucleic Acids Res. 46, W296–W303. [PubMed: 29788355]

Wieczorek M, Urnavicius L, Ti S-C, Molloy KR, Chait BT, and Kapoor TM (2020). Asymmetric Molecular Architecture of the Human γ-Tubulin Ring Complex. Cell 180, 165–175.e16. [PubMed: 31862189]

Williams CJ, Headd JJ, Moriarty NW, Prisant MG, Videau LL, Deis LN, Verma V, Keedy DA, Hintze BJ, Chen VB, et al. (2018). MolProbity: More and better reference data for improved all-atom structure validation. Protein Sci. 27, 293–315. [PubMed: 29067766]

Wood CW, and Woolfson DN (2018). CCBuilder 2.0: Powerful and accessible coiled-coil modeling. Protein Sci. 27, 103–111. [PubMed: 28836317]

Wu S, and Zhang Y (2007). LOMETS: a local meta-threading-server for protein structure prediction. Nucleic Acids Res. 35, 3375–3382. [PubMed: 17478507]

Zheng Y, Wong ML, Alberts B, and Mitchison T (1995). Nucleation of microtubule assembly by a gamma-tubulin-containing ring complex. Nature 378, 578–583. [PubMed: 8524390]

Zheng SQ, Palovcak E, Armache J-P, Verba KA, Cheng Y, and Agard DA (2017). MotionCor2: anisotropic correction of beam-induced motion for improved cryo-electron microscopy. Nat. Methods 14, 331–332. [PubMed: 28250466]

Zivanov J, Nakane T, Forsberg BO, Kimanius D, Hagen WJ, Lindahl E, and Scheres SH (2018). New tools for automated high-resolution cryo-EM structure determination in RELION-3. eLife 7, e42166. [PubMed: 30412051]

Highlights

- Identification and de novo models of MZT1 and MZT2 in the native γ-TuRC
- MZT1 and MZT2 form structurally mimetic subcomplexes with different GCP-NHDs
- MZT1/GCP3-NHD and MZT1/GCP6-NHD occupy the γ-TuRC lumenal bridge
- MZT2/GCP2-NHD interacts with the γ-TuNA peptide on the outer face of the γ-TuRC

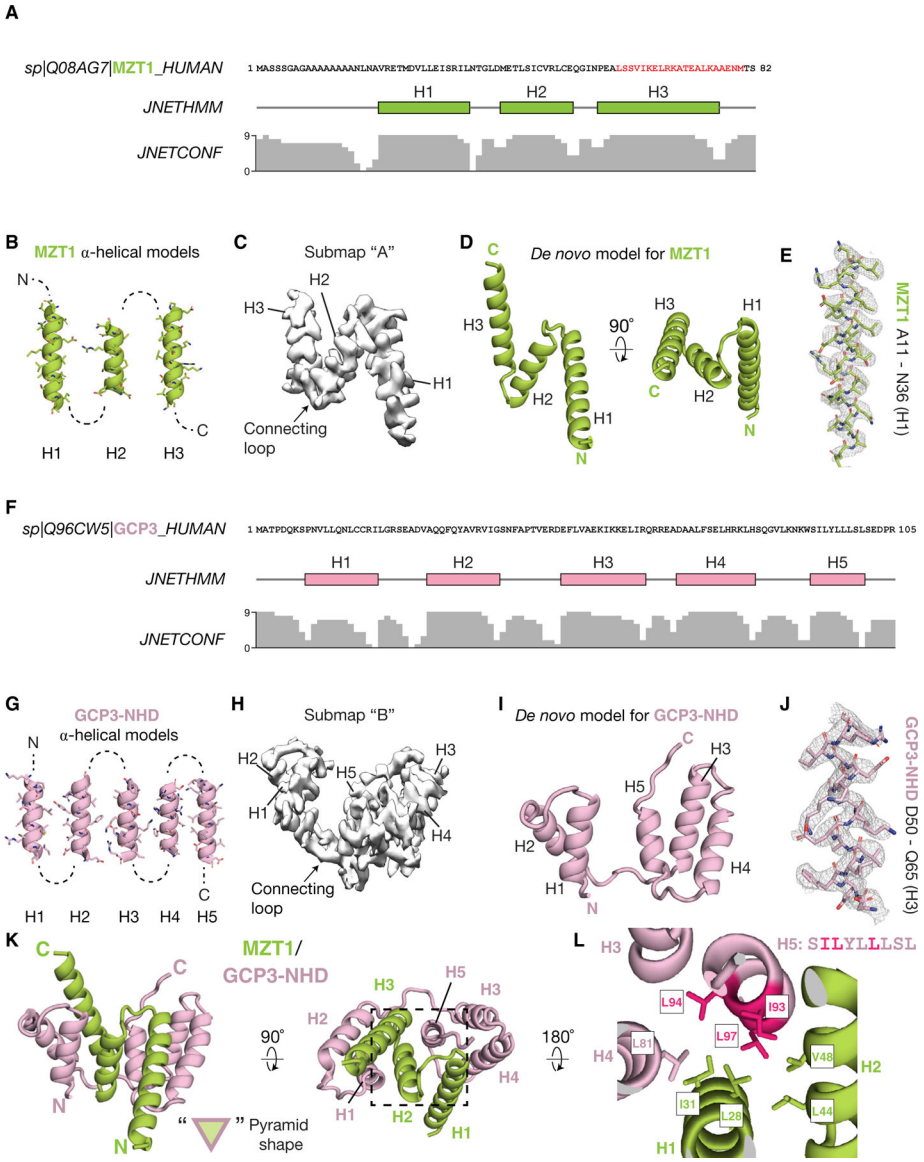

Figure 1. De Novo Structural Model for MZT1 in Complex with GCP3-NHD in the γ-TuRC Lumen

(A) Secondary structure prediction of human MZT1. Top: primary sequence (red, predicted coiled-coil); middle: JNETHMM prediction (Drozdetskiy et al., 2015); bottom: confidence score. α helices H1–H3 are shown as green bars.

(B) Cartoon representation of initial models for MZT1 helices H1–H3. Dotted lines indicate connectivities between α helices.

(C) Surface representation of segmented cryo-EM density submap "A" with α-helical segments and a well-resolved connecting loop indicated.

(D) Two views of a *de novo* molecular model for MZT1 (green cartoon representation).

(E) Example of the fit of MZT1 side chains (stick representation) into the corresponding cryo-EM density (mesh representation).

(F) Secondary structure prediction of GCP3-NHD, displayed as in (A).

(G) Cartoon representation of initial models for GCP3-NHD helices H1–H5 (pink). Dotted lines indicate connectivities between α helices.
(H) Surface representation of segmented cryo-EM density submap B with α-helical segments and a well-resolved connecting loop indicated.
(I) *De novo* molecular model for GCP3-NHD (pink cartoon representation).
(J) Example of the fit of GCP3-NHD side chains (stick representation) into the corresponding cryo-EM density (mesh representation).
(K) Two views of the MZT1/GCP3-NHD subcomplex. The “pyramid shape” of the subcomplex is schematized as a triangle at the bottom of the figure.
(L) Zoom-in view of the region highlighted in
(K) (dashed rectangle) showing hydrophobic residues (stick representation) forming part of the MZT1-GCP3-NHD interface.
See also Figures S1–S3; Tables S1 and S2; Data S1.

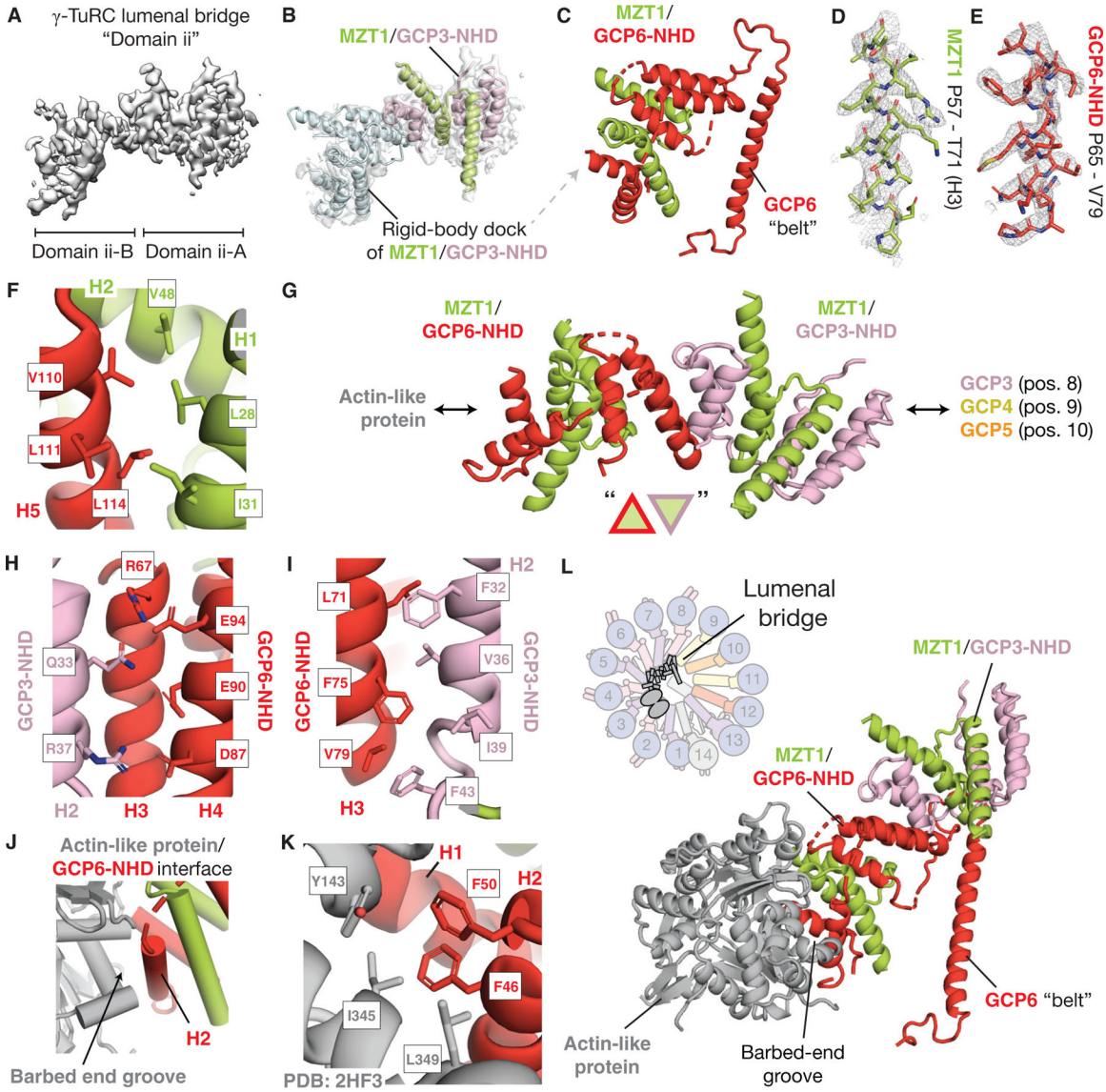

Figure 2. A Second Copy of MZT1 Complexed with GCP6-NHD Is Found in the γ-TuRC Lumen

(A) Surface representation of domains ii-A and ii-B of the γ-TuRC lumenal bridge density.

(B) Models for MZT1 (green cartoon representation) and GCP3-NHD (pink cartoon representation) in domain ii-A and a rigid-body fit of a second copy of MZT1/GCP3-NHD (light blue cartoon representation) docked into domain ii-B (transparent surface representation).

(C) *De novo* molecular model for MZT1 (green cartoon representation) in complex with GCP6-NHD (red cartoon representation). A model for the GCP6 belt is also shown.

(D and E) Examples of the fit of modeled side chains (stick representations) for MZT1 (D) and GCP6-NHD (E) into the corresponding density map (mesh representations).

(F) Zoom-in view highlighting hydrophobic residues (stick representation) that form part of the MZT1/GCP6-NHD interface.

(G) Cartoon representation of MZT1/GCP3-NHD interacting with MZT1/GCP6-NHD within the lumenal bridge. Triangles indicate the pseudo-C1 symmetry formed by the two subcomplexes.

(H and I) Zoom-in views highlighting (H) polar and (I) nonpolar residues that form part of the GCP3-NHD-GCP6-NHD interface.

(J) Cartoon representation of the actin-like protein/GCP6-NHD interface.

(K) Zoom-in view highlighting residues that form part of the GCP6-NHD-actin-like protein interface.

(L) Top left: schematic of the γ-TuRC. Bottom right: cartoon representation of the γ-TuRC lumenal bridge model, including the GCP6 belt. γ-TuRC subunits are colored as in Wieczorek et al. (2020).

See also Figures S1–S3; Tables S1 and S2; Data S1.

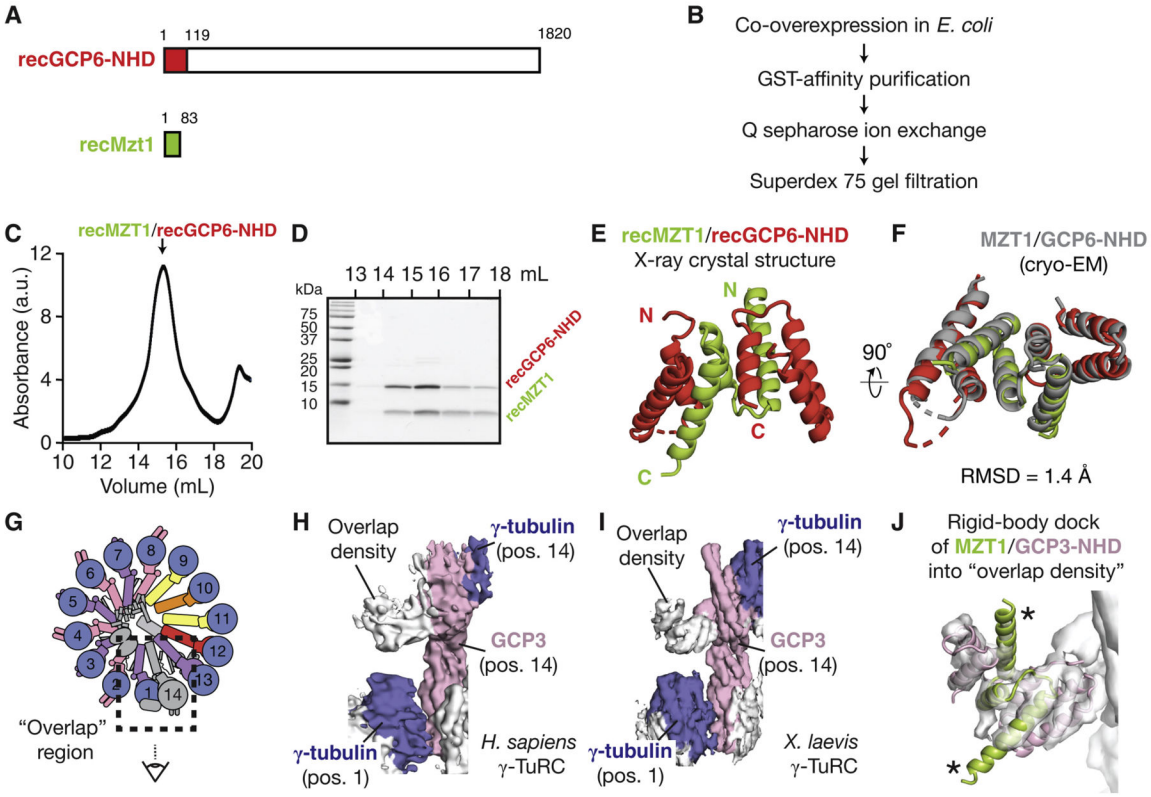

Figure 3. Structure of Reconstituted MZT1/GCP6-NHD and Identification of a Third MZT/GCP-NHD-like Subcomplex at the γ-TuRC Overlap

(A) Schematics of GCP6 and MZT1. The recGCP6 (red rectangle) and recMzt1 (green rectangle) sequences are indicated.

(B) The recMZT1/recGCP6-NHD purification strategy.

(C) Superdex 75 10/300 GL elution profile for recMZT1/recGCP6-NHD.

(D) Peak fractions in (C) resolved by SDS-PAGE and stained with Coomassie blue.

(E) Cartoon representation of the recMZT1 (green)/recGCP6-NHD (red) X-ray crystal structure.

(F) The recMZT1/recGCP6-NHD X-ray crystal structure aligned to cryo-EM model of MZT1/GCP6-NHD (gray).

(G) Schematic of the native human γ-TuRC establishing the viewing angle in (H)–(J). Subunits are colored as in Wieczorek et al. (2020).

(H and I) Surface representation view of (H) EMDB: EMD-20170 (Wieczorek et al., 2020) and (I) EMDB: EMD-10491 (Liu et al., 2020) viewed from the angle in (G). Only surfaces corresponding to models of GCP3 at position 14 and γ-Tubulins at positions 1 and 14 are colored.

(J) Rigid-body docking of MZT1/GCP3-NHD (cartoon representation) into the overlap density of EMDB: EMD-10491 (transparent surface representation) (Liu et al., 2020). Asterisks highlight MZT1 helices H1 and H3.

See also Table S3.

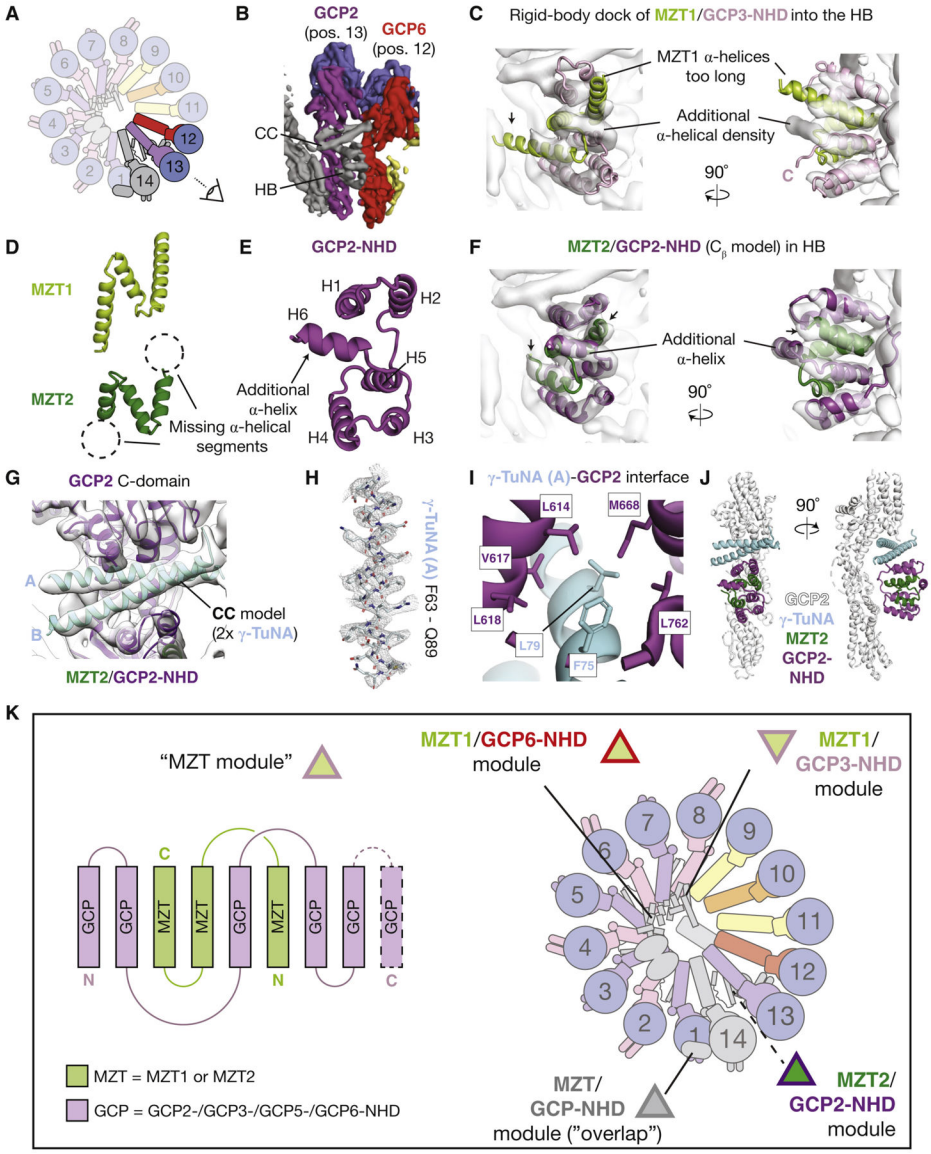

Figure 4. MZT2/GCP2-NHD Interact with the γ-TuNA Peptide on the Outer Face of the γ-TuRC

(A) Schematic of the γ-TuRC highlighting subunits from positions 12–14 and indicating the viewing angle in (B). Subunits are colored as in Wieczorek et al. (2020).

(B) Surface representation view of EMDB: EMD-21070 (Wieczorek et al., 2020) indicating the location of the CC and HB densities.

(C) Two views of the MZT1/GCP3-NHD model (cartoon representation) rigid-body docked into the HB. Mismatches between the MZT1/GCP3-NHD model and the HB density are indicated (text and arrow).

(D) Cartoon representations of MZT1 (top, light green) and a *de novo* model for MZT2 (bottom, dark green). Dashed circles indicate α-helical regions of MZT1 that are not present in the MZT2 model.

(E) Cartoon representation of a *de novo* model for GCP2-NHD. The additional C-terminal α-helix that is not present in GCP3-NHD is indicated.

(F) Model for MZT2/GCP2-NHD (dark green and purple cartoon representations) in the HB density (transparent surface).
(G) Model for the γ-TuNA coiled-coil (light blue cartoon representation) in the CC density (transparent surface). Models for the GCP2 C-domain and MZT2/GCP2-NHD are also shown for reference.
(H) Example of the fit of γ-TuNA helix A side chains (stick representation) in the corresponding density map (mesh representation).
(I) Zoom-in view highlighting hydrophobic residues (stick representations) at the γ-TuNA helix A/GCP2 C-domain interface.
(J) Two views in cartoon representation of the tripartite γ-TuNA/MZT2/GCP2-NHD subcomplex bound to the GCP2 stalk model at position 13 of the γ-TuRC.
(K) MZT proteins form multi-facedted structural modules in the γ-TuRC. Left: schematic of the MZT module comprising three α helices from MZT1 or MZT2 intercalated with at least five α helices contributed by either GCP2-, GCP3-, GCP5-, or GCP6-NHDs. GCP5 is included in this list based on similar secondary structure predictions to other GCP-NHDs. Right: schematic of the γ-TuRC highlighting the locations of the four MZT modules identified in this study. MZT modules are schematized with triangles outlined in the color corresponding to the GCP making up the module, according to the coloring scheme used in this study (Figures 1, 2, 3, and 4).
See also Figures S1, S2, and S4; Tables S1 and S3; Data S1.

KEY RESOURCES TABLE

REAGENT or RESOURCE	SOURCE	IDENTIFIER
Antibodies		
Anti-y-tubulin, mouse monoclonal, clone GTU-88	Millipore-Sigma	Cat# T6557
Bacterial and Virus Strains		
DH5α	ThermoFisher	Cat# 18265017
Rosetta	Novagen	Cat# 71400
BL21-CodonPlus (DE3)-RIL	Stratagene	Cat# 230245
Biological Samples		
HeLa S3 cytoplasmic extract, gift from Robert Roeder	(Abmayr and Carrozza, 2001)	N/A
Purified native y-tubulin ring complex from HeLa S3 cells	This study	N/A
Chemicals, Peptides, and Recombinant Proteins		
Recombinant GFP nanobody	This study	N/A
Recombinant GFP-y-TuNA	This study	N/A
Guanosine 5'-triphosphate, Disodium salt trihydrate	Jena Bioscience	Cat#NU-1012
complete EDTA-free Protease Inhibitor Cocktail	Roche	Cat# 11873580001
IPTG	Gold Biotechnology	Cat# 12481C
Dithiothreitol (DTT)	Gold Biotechnology	Cat# DTT25
L-Glutathione reduced	Gold Biotechnology	Cat#G155500
PreScission protease	In-house	N/A
TEV protease	In-house	N/A
Recombinant recMZT1/recGCP6-NHD	This study	N/A
Critical Commercial Assays		
Hapmton crystal screen: SaltRxi	Hampton Research	Cat#HR2–107
Glutathione Agarose	GE Healthcare Life Sciences	Cat#17075604
CloneAmp HiFi PCR Premix	Takara Bio.	Cat#639298
In-Fusion HD Cloning Plus	Takara Bio.	Cat#638920
Deposited Data		
Focused refinement γ-TuRC density map corresponding to the lumenal bridge	This study	EMD-21984
Focused refinement γ -TuRC density map surrounding positions 12 and 13	This study	EMD-21985
Structural models of the γ-TuRC lumenal bridge domain ii proteins: MZT1/GCP3-NHD and MZT1/GCP6-NHD (including GCP6 "belt")	This study	PDB ID 6X0U
Structural models of MZT2/GCP2-NHD and the y-TuNA coiled-coil at position 13 of the γ-TuRC	This study	PDB ID 6X0V
Structural model recMZT1/recGCP6-NHD determined by X-ray crystallography	This study	PDB ID 6M33
Oligonucleotides		
Primers for/isGCP6(1 −119) F GGGGCCCCTGGGAT CCATGGCTAGTATAACCCAGC	This study	N/A

REAGENT or RESOURCE	SOURCE	IDENTIFIER
Primers for/7sGCP6(1 −119) R GGCCGCTCGAGTCGA CTTAACCGGCCAGCTGAAC	This study	N/A
Primers for *hs*MZT1 F TCCAGGGGCCCCATATGGCG AGTAGCAGCGGT	This study	N/A
Primers for *hs*MZT1 R GGTGGTGGTGCTCGAGTCAG CTTGTCATATTTTCAGC	This study	N/A
Recombinant DNA		
Bacterial expression vector for anti-GFP nanobodyclone LG-16, gift from Michael Rout	Fridyetal., 2014	N/A
pET His6 Sumo TEV LIC cloning vector (1S), gift from Scott Gardia	Addgene (Unpublished)	pET His6 Sumo TEV LIC cloning vector (1S) Addgene plasmid # 29659; http://addgene.org/29659; RRID:Addgene_29659
pRcCMV Cep215, gift from Erich Nigg	Graser S, Stierhof YD, Nigg EA J Cell Sci. 2007 Dec 15;120(Pt 24):4321–31. Epub 2007 Nov 27.	pRcCMV Cep215 (Nigg CW493) Addgene plasmid #41152; http://addgene.org/41152; RRID:Addgene_41152
pMW96 - pET expression vector for His6-SUMO- TEV-GFP-PreScission-Y-TuNA	Wieczorek et al., 2020	N/A
Expression plasmid for hsGCP5-NTD	This study	N/A
Expression plasmid for hsMzti Software and Algorithms	This study	N/A
Software and Algorithms		
RELION	Zivanov et al., 2018	https://www3.mrc-lmb.cam.ac.uk/relion/index.php?title=Main_Page
EMAN2	Tang et al., 2007	https://blake.bcm.edu/emanwiki/EMAN2
Coot	Emsley etal., 2010	https://www2.mrc-lmb.cam.ac.uk/personal/pemsley/coot/
UCSF Chimera	Pettersen et al., 2004	https://www.cgl.ucsf.edu/chimera/
Phenix	Williams et al., 2018	https://www.phenix-online.org
PyMol	The PyMOL Molecular Graphics System, Version 2.0 Schrbdinger, LLC.	https://pymol.org/2/
Serial EM	Mastronarde, 2005	https://bio3d.colorado.edu/SerialEM/
MotionCor2	Zheng et al., 2017	https://emcore.ucsf.edu/ucsf-motioncor2
CTFFIND4	Rohou and Grigorieff, 2015	https://grigoriefflab.umassmed.edu/ctffind4
HKL2000	HKL Research, Inc.	https://www.hkl-xray.com/
Other		
HiTrap NHS-Activated HP	GE Healthcare	Cat# 17071601
Superdex75 10/300 GL	GE Healthcare Life Sciences	Cat#GE17517401
HiLoad 16/60 Superdex 75 prep grade	GE Healthcare Life Sciences	Cat#GE17106801
HiTrap Q HP	GE Healthcare Life Sciences	Cat#GE29051325